Supplementary Information

All-solid-state electrochromic devices based on the ultra-thin Li_3PO_4 electrolyte

Jiuyong Li,[a,b] Weiming Liu,[a,b] Youxiu Wei,[a,b] Xueting Xu [c] and Yue Yan *[a,b]

a Baimtec Material Co., LTD., Beijing, 100095, China

b Beijing Engineering Research Center of Advanced Structural Transparence for the Modern Trafffc System, Beijing, 100095, China

c Faculty of Materials Science and Engineering, Shenyang Aerospace University, Shenyang, 110136, China.

*Corresponding author. E-mail: 15737936609@163.com

Content:

Experimental Section

Preparation of films and ECD

The inorganic all-solid-state ECD, with a layer structure of glass/ITO/WO_3/Li/Li_3PO_4/NiO/ITO, was fabricated on 4 × 5 cm ITO-coated glass substrates (sheet resistance: 7 Ω/sq) via magnetron sputtering. The deposition of each layer was carried out sequentially at room temperature under a continuous vacuum environment. The mobile Li^+ ions in this device structure are supplied by the sputtered metallic Li; therefore, the ultra-thin Li_3PO_4 electrolyte thickness essentially does not limit the total amount of mobile ions.

Prior to film deposition, the ITO/glass substrates were cleaned ultrasonically in anhydrous ethanol and deionized water for 10 min, followed by drying with nitrogen gas. To prevent cross-contamination, each sputtering target (74.5 mm in diameter) was fitted with a protective cover. The targets employed were Ni, Li_3PO_4, W, Li, and ITO (In_2O_3:SnO_2 = 90:10 wt%), positioned approximately 10 cm from the substrate. During the fabrication process, the chamber was evacuated to a base pressure of 2×10^{-4} Pa, and each target was pre-sputtered for about 10 min before deposition. The substrate holder was continuously rotated to ensure film uniformity. Gas flow rates for Ar (99.999%), O_2 (99.999%), and an Ar–O_2 mixture (90% Ar + 10% O_2, 99.999%) were precisely controlled using mass flow controllers. The Ar–O_2 mixture was used during the deposition of NiO and ITO layers to enable accurate regulation of the low oxygen flow required. Detailed deposition parameters are summarized in Table S1. After fabrication, the sample was sectioned into four identical devices, each measuring 2 × 2.5 cm², to ensure consistency in subsequent characterization and testing. For structural analysis of individual layers, corresponding films were deposited on silica glass substrates under identical conditions used for the full ECD.

Table S1 Detailed deposition parameters of the all-solid-state ECD.

Film	Target	Power source	Ar: O_2: Ar-O_2[a] (sccm)	Working Pressure (Pa)	Sputtering power (W)	Thickness (nm)
ITO	ITO	DC	24.6:0:6	0.5	120	150
NiO	Ni	p-DC	11:0:14	2	130	150
Li_3PO_4	Li_3PO_4	RF	30:0:0	0.3	80	~12
WO_3	W	p-DC	32:8:0	1.5	120	300
Li	Li	DC	30:0:0	0.5	60	40

[a] Ar-O_2 mixture (90% Ar+10% O_2).

Characterization and electrochemical measurements

The phase structures of each thin film layer in the ECD were examined by X-ray diffraction (XRD, λ = 0.15418 nm, Bruker D8 Advance). The surface morphology of the films was characterized using scanning electron microscope (SEM, Hitachi SU-8010). The surface roughness of each layer in the ECD was measured by atomic force microscope (AFM, Bruker Dimension) operating in tapping mode. The thickness of the Li_3PO_4 thin film and the cross-sectional morphology of the device were determined by transmission electron microscope (TEM, FEI Tecnai G2 F30) and SEM. The TEM specimen of the device was prepared using focused ion beam (FIB, FEI Helios Nanolab600i dual beam). The chemical composition of the Li_3PO_4 thin film was characterized by XPS (XPS, ESCALAB 250Xi).

The electrochemical and electrochromic properties of the devices were measured using an electrochemical workstation (CHI 660E). In order to prevent the leakage current caused by edge shorts, all edges were cut off 1–2 mm width. Electrochemical impedance spectroscopy (EIS) was performed on the device with an AC voltage of 5 mV amplitude and a frequency range from 0.1 Hz to 10^5 Hz. Cyclic voltammetry (CV) tests were conducted within a voltage range of -1.8 to 1.5 V at a scan rate of 50 mV/s. The cycling stability of the devices was evaluated through chronoamperometry (CA) cycles, with applied voltages and durations of -1.8 V for 40 s during coloration and 1.5 V for 30 s during bleaching. The transmittance spectra of the devices in the colored and bleached states were measured using a UV-Vis-NIR spectrophotometer (Agilent Cary 5000) over a wavelength range of 380-800 nm. The in-situ variation in transmittance of the ECD over time was also recorded using the spectrophotometer.

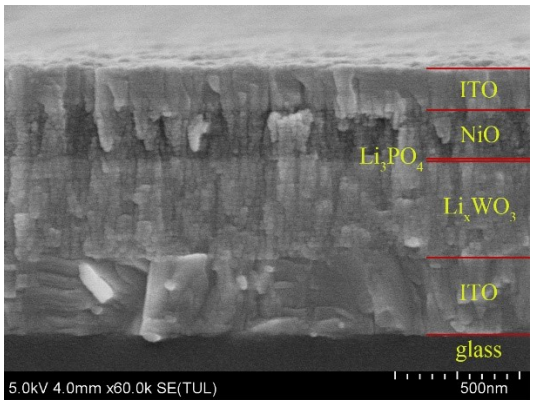

Fig. S1 Cross-sectional SEM image of the all-solid-state ECD

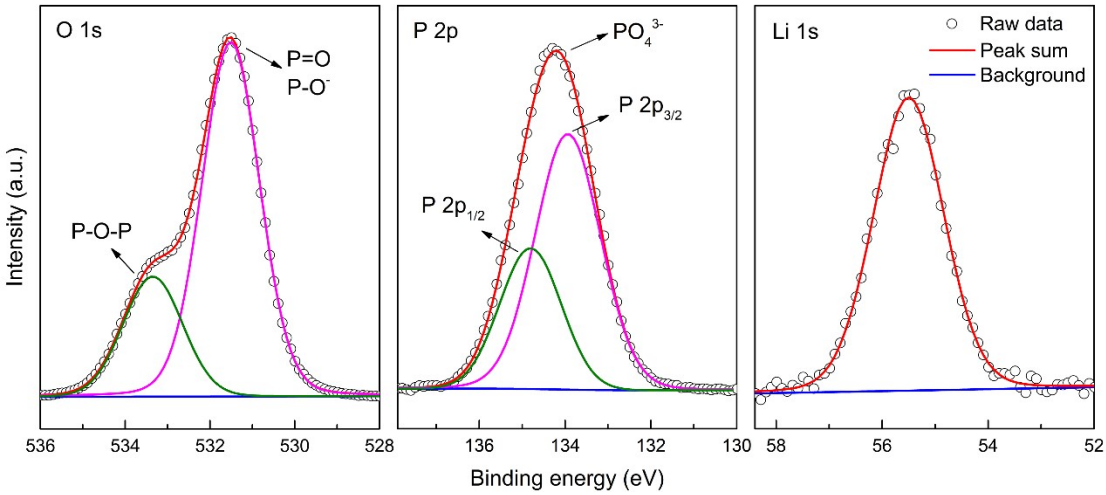

Fig. S2 XPS spectra of O 1s, P 2p and Li 1s core levels of the Li_3PO_4 layer

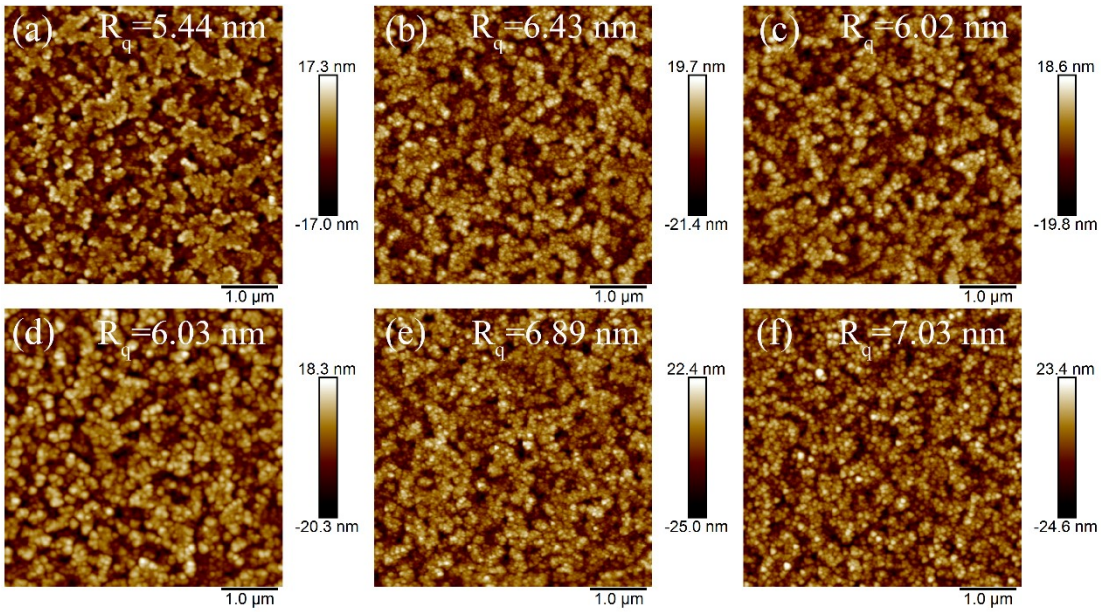

Fig. S3 AFM images of the films (a) glass/ITO, (b) glass/ITO/WO_3, (c) glass/ITO/WO_3/Li, (d) glass/ITO/WO_3/Li/Li_3PO_4, (e) glass/ITO/WO_3/Li/Li_3PO_4/NiO, and (f) glass/ITO/WO_3/Li/Li_3PO_4/NiO/ITO

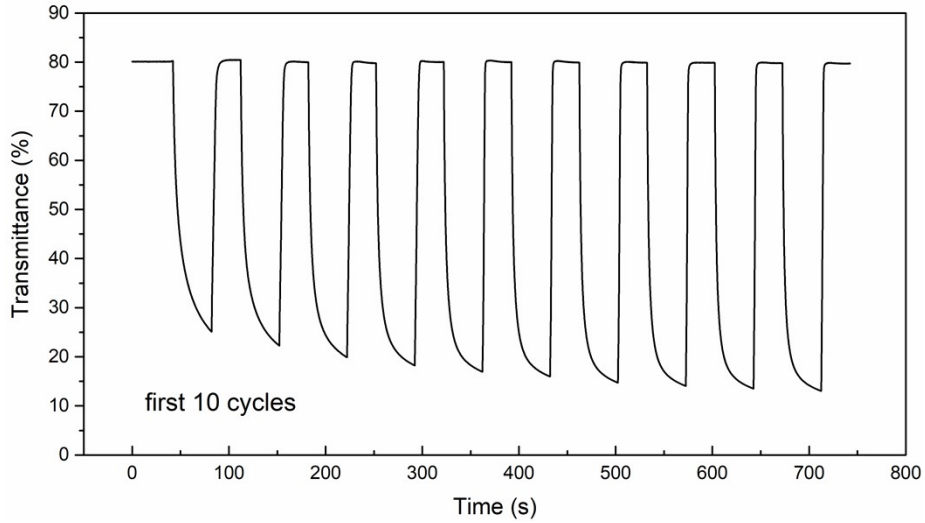

Fig. S4 Transmittance variation curves of the ECD during the first 10 cycles of CA measurement

Typically, ECDs undergo a characteristic electrochemical activation process in the initial cycles, during which the ion insertion/extraction behavior is not yet fully stabilized, leading to transient performance fluctuations. As shown in Fig. S4, during the first 10 cycles, the bleached-state transmittance of the device remains nearly constant, while the colored-state transmittance gradually decreases and then stabilizes, corresponding to a progressive deepening of coloration until saturation. This phenomenon is primarily attributed to the gradual penetration and full insertion of electrolyte ions into the electrochromic film in the early cycles, which fills the incompletely connected ion transport pathways and enables more active sites to participate in the electrochromic reaction, thereby improving the coloration efficiency and manifesting as a reduction in colored-state transmittance. As the cycles proceed, the ion insertion/extraction gradually reaches a reversible equilibrium, and the device performance becomes stable. Therefore, to more accurately evaluate the long-term cycling stability of the device, we selected the 10th cycle data after nearly completing the activation process as the performance baseline for the initial stage, to eliminate the non-steady-state influence caused by the initial conditioning process.

Table S2. Summary of inorganic all-solid-state ECDs based on various electrolyte layers in recent years.

Ref.	Structure of ECDs	Electrolyte thickness[a] (nm)	ΔT_{max} (%)	t_c/t_b (s)	CE ($cm^2 \cdot C^{-1}$)	Cycling stability[b]
1	glass/ITO/NiO/Si_3N_4/Li_xMg_yN/WO_3/ITO	450	40	-	77.0	57.5% after 1000 CA cycles
2	glass/ITO/NiO_x:H/ZrO_2/WO_3/ITO	-	68	70/42	-	100% after 25 cycles
3	PET/ITO/NiO_x/Ta_2O_5:H/WO_3/ITO	247	60	-	-	100% after 125 cycles
4	PET/ITO/NiO_x/$LiTaO_3$/WO_3/ITO	-	65.2	7/55	68.5	-
5	glass/ITO/NiO_x/$LiTaO_3$/WO_3/ITO	440	67	85/42	-	-
6	glass/ITO/NiO_x/Ta_2O_5/$LiNbO_3$/Ta_2O_5/WO_3/ITO	560	52.5	21/21	98.0	64% after 10000 cycles
7	glass/ITO/NiO/Si_3N_4/$LiNbO_3$/Si_3N_4/WO_3/ITO	290	43	-	-	100% after 100 cycles
8	glass/ITO/NiO/ZrO_2/Li/WO_3/ITO	100	64.9	48/6	106.6	98% after 4000 cycles[c]
9	glass/ITO/WO_3/$LiNbO_3$/Al-$LiNiO_x$/ITO	426	45	17.9/4.1	55	77.8% after 10000 cycles
10	glass/ITO/NiO/Ta_2O_5/WO_3/ITO	130	50	13/5	-	89% after 2000 cycles
11	glass/ITO/WO_3/LiF/NiO/ITO	90	58.9	9.6/4	88.5	99% after 300 cycles
12	glass/ITO/NiO/Ta_2O_5/$LiAlSiO_4$/Ta_2O_5/WO_3/ITO	120	50.8	25/32.7	60.3	81.5% after 1000 cycles
13	glass/ITO/WO_3/MgF_2/NiO/ITO	230	66.4	19.2/8.3	27.7	-
14	glass/ITO/WO_3/CaF_2/NiO/ITO	185	38.8	22.8/2.8	52.4	62.2% after 125 cycles
15	glass/ITO/NiO_x/LiPON/WO_3/ITO	450	68.4	27	-	89.9% after 200 cycles
16	glass/ITO/WO_3/Al_2SiO_5/NiO_x/ITO	80	44.58	14.8/3.7	98.17	94.2% after 70 cycles
17	glass/ITO/WO_3/Li/Ta_2O_5/NiO/ITO	450	44.9	5.1/0.9	65.2	86.1% after 1000 cycles
This work	**glass/ITO/WO_3/Li/Li_3PO_4/NiO/ITO**	**~12**	**69.5**	**9.7/2.5**	**76.4**	**89.9% after 1000 cycles**

[a] If the device contains an electron-blocking layer, it is also considered part of the electrolyte layer, as it effectively serves to conduct ions and block electrons.

[b] Defined as the percentage of ΔT after the cycle to the initial ΔT.

[c] It is expressed as the percentage of ΔT after the cycle to the maximum ΔT.

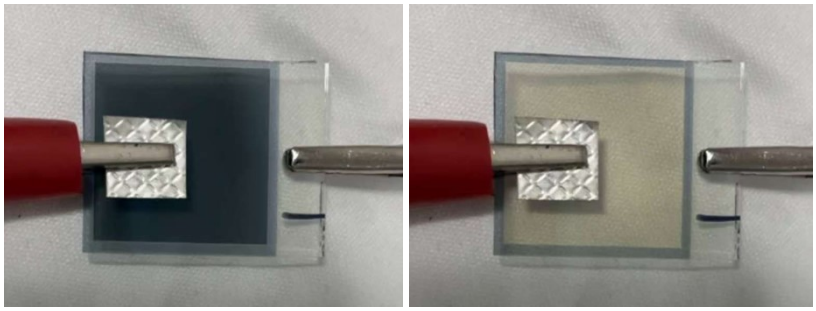

Fig. S5 Photographs of the ECD in the colored and bleached states.

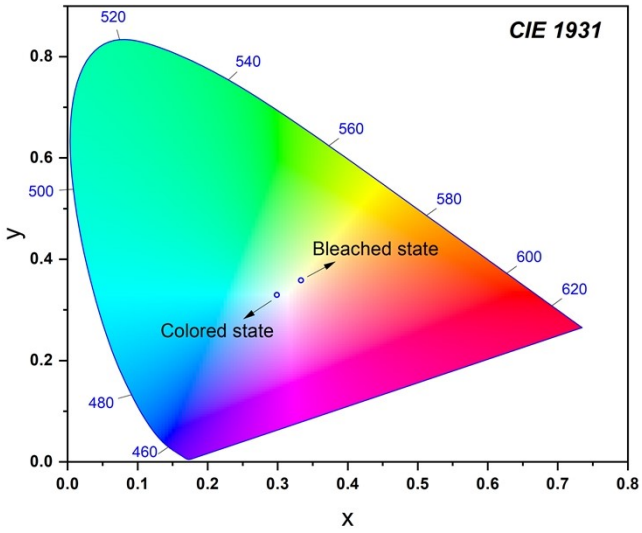

Fig. S6 CIE chrominance coordinates of the ECD in colored and bleached states.

Table S3. Color parameters of the ECD in bleached and colored states

	*L**	*a**	*b**	*ΔE*
Colored state	40.52	-3.93	-1.06	50.62
Bleached state	88.90	-3.45	13.83	

The electrochromic performance of the device was quantitatively characterized using the CIE 1931 chromaticity diagram and the CIE L*a*b* color space. As shown in the Fig. S6 and Table S2, the colored state exhibited CIE L*a*b* coordinates of L*=40.52, a*=−3.93, and b*=−1.06, corresponding to a low-luminance, neutral blue-green hue. Upon bleaching, the values shifted to L*=88.9, a*=−3.45, and b*=13.83, with a substantial increase in luminance and a movement of the chromaticity coordinates toward the white light region in the CIE 1931 diagram. The total color difference (ΔE) between the two states, calculated by the formula:

$$\Delta E=\sqrt{[(L^*_{bl}-L^*_{col})^2+(a^*_{bl}-a^*_{col})^2+(b^*_{bl}-b^*_{col})^2]}$$

was found to be approximately 50.62, indicating a high optical contrast between the colored and bleached states. Notably, the color change was dominated by luminance modulation with negligible chromaticity shift, demonstrating outstanding neutral-tone electrochromic characteristics that meet the requirements of low chromatic interference and high transmittance modulation for applications such as smart windows.

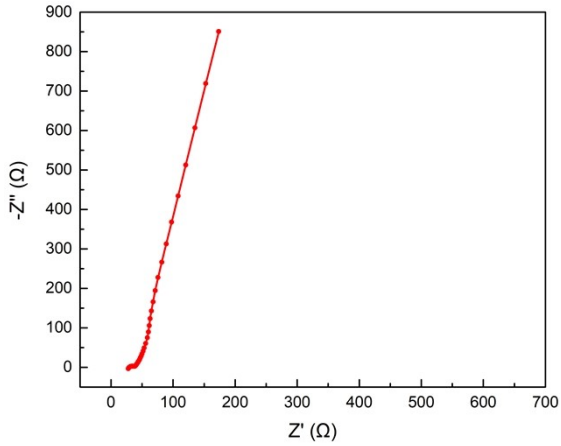

Fig. S7 Nyquist plot of the all-solid-state ECD.

Electrochemical impedance spectroscopy (EIS) measurements were performed on the fabricated all-solid-state ECD. The resulting Nyquist plot is presented in Fig. S7. The spectrum consists of a small depressed semicircle at high-to-intermediate frequencies, followed by a Warburg-type diffusion tail at low frequencies.

Given the multi-layered architecture of the device (glass/ITO/WO_3/Li/Li_3PO_4/NiO/ITO), the impedance response arises from overlapping contributions: (1) ohmic resistance of the electrodes and the electrolyte, (2) charge-transfer resistance at the WO_3/electrolyte and electrolyte/NiO interfaces, and (3) solid-state diffusion of Li^+ ions. Due to the superposition of these processes, it is not possible to unambiguously resolve the intrinsic ionic conductivity of the Li_3PO_4 electrolyte or the Li^+ diffusion coefficient in the WO_3 layer from this full-device measurement alone. Nonetheless, the characteristic Warburg tail confirms the occurrence of Li^+ diffusion processes, and the overall impedance behavior is consistent with the device's fast switching speed and high coloration efficiency, indirectly supporting efficient Li^+ transport across the ultrathin Li_3PO_4 electrolyte and within the electrochromic layer.

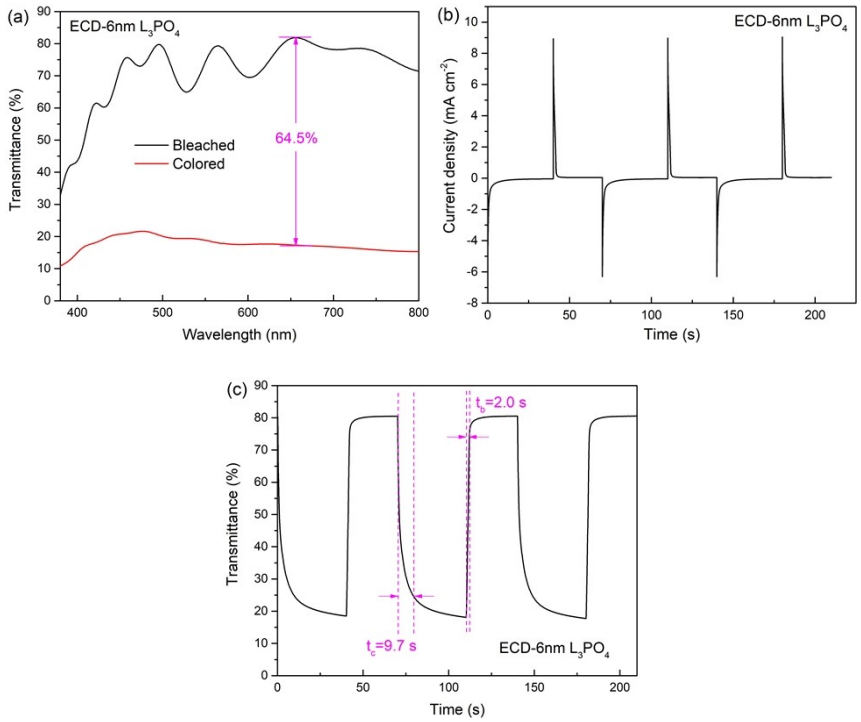

Fig. S8 (a) The transmittance spectra, (b) current density-time curve of the ECD with ~ 6 nm Li_3PO_4 and (c) corresponding in-situ transmittance measurements at 655 nm.

To further verify the feasibility of the ultrathin electrolyte strategy, an ECD with a 6 nm-thick Li_3PO_4 electrolyte was prepared. As shown in Fig. S8, the device exhibits an optical modulation depth of 64.5%, coloration/bleaching response times of 9.7 s and 2.0 s, and leakage current densities of 41.3 μA cm^{-2} and 43.5 μA cm^{-2} in the colored and bleached states, respectively. The performance is comparable to that of the ~12 nm device, with only a slight decrease in optical modulation and a slight increase in leakage current. This is very likely because the underlying Li_xWO_3 layer has a root-mean-square roughness of 6.02 nm (Fig. S3c), which increases the probability of pinholes and defects in the extremely thin 6 nm Li_3PO_4 layer, thereby slightly weakening its electron-blocking capability. These results further support the reliability and generality of our ultrathin electrolyte approach.

REFERENCES

(1) Xiao, Y.; Dong, G.; Huang, Q.; Liu, Q.; Guo, J.; Liu, J.; Zhang, J.; Diao, X. Electro-optical performance of inorganic monolithic electrochromic device with a pulsed DC sputtered Li_xMg_yN ion conductor. J. Solid State Electrochem. 2017, 22 (1), 275-283.

(2) Dong, D.; Wang, W.; Dong, G.; Zhou, Y.; Wu, Z.; Wang, M.; Liu, F.; Diao, X. Electrochromic properties of NiO :H films deposited by DC magnetron sputtering for ITO/NiO :H/ZrO_2/WO_3/ITO device. Appl. Surf. Sci. 2015, 357, 799-805.

(3) Dong, D.; Wang, W.; Dong, G.; Zhang, F.; He, Y.; Yu, H.; Liu, F.; Wang, M.; Diao, X. Electrochromic properties and performance of NiO_x films and their corresponding all-thin-film flexible devices preparedby reactive DC magnetron sputtering. Appl. Surf. Sci. 2016, 383, 49-56.

(4) Liu, Q.; Dong, G.; Xiao, Y.; Gao, F.; Wang, M.; Wang, Q.; Wang, S.; Zuo, H.; Diao, X. An all-thin-film inorganic electrochromic device monolithically fabricated on flexible PET/ITO substrate by magnetron sputtering. Mater. Lett. 2015, 142, 232-234.

(5) Song, X.; Dong, G.; Gao, F.; Xiao, Y.; Liu, Q.; Diao, X. Properties of NiO_x and its influence upon all-thin-film ITO/NiO_x/$LiTaO_3$/WO_3/ITO electrochromic devices prepared by magnetron sputtering. Vacuum 2015, 111, 48-54.

(6) Liu, Q.; Dong, G.; Chen, Q.; Guo, J.; Xiao, Y.; Delplancke-Ogletree, M.-P.; Reniers, F.; Diao, X. Charge-transfer kinetics and cyclic properties of inorganic all-solid-state electrochromic device with remarkably improved optical memory. Sol. Energy Mater. Sol. Cells 2018, 174, 545-553.

(7) Huang, Q.; Dong, G.; Xiao, Y.; Diao, X. Electrochemical studies of silicon nitride electron blocking layer for all-solid-state inorganic electrochromic device. Electrochim. Acta 2017, 252, 331-337.

(8) Li, W.; Zhang, X.; Chen, X.; Zhao, Y.; Wang, L.; Chen, M.; Li, Z.; Zhao, J.; Li, Y. Lithiation of WO_3 films by evaporation method for all-solid-state electrochromic devices. Electrochim. Acta 2020, 355, 136817.

(9) Wang, C.; Dong, G.; Zhao, Y.; He, Y.; Ding, Y.; Du, X.; Zhong, X.; Wang, M.; Diao, X. Enhanced electrochromic performance on anodic nickel oxide inorganic device via lithium and aluminum co-doping. J. Alloys Compd. 2020, 821, 153365.

(10) Chen, P.-W.; Chang, C.-T.; Ali, M. M.; Wu, J.-Y.; Li, Y.-C.; Chen, M.-H.; Jan, D.-J.; Yuan, C.-T. Tantalum oxide film deposited by vacuum cathodic arc plasma with improved electrochromic performance. Sol. Energy Mater. Sol. Cells 2018, 182, 188-195.

(11) Chen, X.; Dou, S.; Li, W.; Liu, D.; Zhang, Y.; Zhao, Y.; Li, Y.; Zhao, J.; Zhang, X. All solid state electrochromic devices based on the LiF electrolyte. Chem. Commun. 2020, 56 (37), 5018-5021.

(12) Zhao, Y.; Zhang, X.; Chen, X.; Li, W.; Li, Z.; Chen, M.; Sun, W.; Zhao, J.; Li, Y. All-solid-state electrochromic devices based on the $LiAlSiO_4$ electrolyte. Mater. Lett. 2021, 292, 129592.

(13) Chen, X.; Li, W.; Dou, S.; Wang, L.; Zhao, Y.; Zhang, X.; Li, Y.; Zhao, J. MgF_2 as abundant and environmentally friendly electrolytes for high performance electrochromic devices. J. Materiomics 2021, 7 (6), 1318-1323.

(14) Chen, X.; Zhang, H.; Li, W.; Xiao, Y.; Zhang, X.; Li, Y. CaF_2: A novel electrolyte for all solid-state electrochromic devices. Environ. Sci. Ecotechnology 2022, 10, 100164.

(15) H. Wang, J. Wang, Q. Shi, Y. Su, P. Tang, S. Huang, S. Lin, M. Dai. Influence of LiPON thickness on the electro-optical performance of inorganic all-solid-state electrochromic devices. Sol. Energy Mater. Sol. Cells, 2023, 251, 112140.

(16) J. Wang, S. Xie, Q. Shi, H. Wang, H. Yang, S. Lin, M. Dai. Effect of the thicknesses of the Al_2SiO_5

ion conductor on the opto-electrical properties for all-solid electrochromic devices, Ceram. Int., 2022, 48, 31491-31499.
(17) J. Li, Y. Wei, W. Liu, Z. Wang, Y. Yan, Influence of Ta_2O_5 electrolyte thickness on the electro-optical performance of all-solid-state electrochromic devices, J. Phys. Chem. Solids, 2025, 204, 112784.